

MASS ACCRETION AND ITS EFFECTS ON THE SELF-SIMILARITY OF GAS PROFILES IN THE OUTSKIRTS OF GALAXY CLUSTERS

ERWIN T. LAU^{1,2}, DAISUKE NAGAI^{1,2,3}, CAMILLE AVESTRUZ^{1,2}, KAYLEA NELSON^{2,3}, AND ALEXEY VIKHLININ⁴

¹Department of Physics, Yale University, New Haven, CT 06520, USA; erwin.lau@yale.edu

²Yale Center for Astronomy and Astrophysics, Yale University, New Haven, CT 06520, USA

³Department of Astronomy, Yale University, New Haven, CT 06520, USA

⁴Harvard-Smithsonian Center for Astrophysics, 60 Garden Street, Cambridge, MA 02138, USA

Received 2014 November 19; accepted 2015 April 21; published 2015 June 9

ABSTRACT

Galaxy clusters exhibit remarkable self-similar behavior which allows us to establish simple scaling relationships between observable quantities and cluster masses, making galaxy clusters useful cosmological probes. Recent X-ray observations suggested that self-similarity may be broken in the outskirts of galaxy clusters. In this work, we analyze a mass-limited sample of massive galaxy clusters from the *Omega500* cosmological hydrodynamic simulation to investigate the self-similarity of the diffuse X-ray emitting intracluster medium (ICM) in the outskirts of galaxy clusters. We find that the self-similarity of the outer ICM profiles is better preserved if they are normalized with respect to the mean density of the universe, while the inner profiles are more self-similar when normalized using the critical density. However, the outer ICM profiles as well as the location of accretion shock around clusters are sensitive to their mass accretion rate, which causes the apparent breaking of self-similarity in cluster outskirts. We also find that the collisional gas does not follow the distribution of collisionless dark matter (DM) perfectly in the infall regions of galaxy clusters, leading to 10% departures in the gas-to-DM density ratio from the cosmic mean value. Our results have a number implications for interpreting observations of galaxy clusters in X-ray and through the Sunyaev–Zel’dovich effect, and their applications to cosmology.

Keywords: cosmology: theory – galaxies: clusters: general – galaxies: clusters: intracluster medium – methods: numerical

1. INTRODUCTION

Galaxy clusters are the most massive gravitationally bound objects in the universe. Most of the baryons are in the form of hot X-ray emitting gas and reside in the deep gravitational potential wells of galaxy clusters. The hot gas is detectable in both the X-ray and the microwave, through the Sunyaev–Zel’dovich (SZ) effect. Observations of the intracluster medium (ICM) show remarkable regularity over a wide range of mass and redshift, making galaxy clusters powerful probes for cosmology (e.g. Allen et al. 2011, for review).

Self-similarity is a generic prediction of gravitational structure formation. It features simple scaling relations between the observable properties and mass of galaxy clusters (Kaiser 1986; Voit 2005; Kravtsov & Borgani 2012, for a recent review). When scaled by cluster mass, the radial profiles of thermodynamic properties of the ICM display remarkable resemblance (Vikhlinin et al. 2006; Nagai et al. 2007; Pratt et al. 2009; Arnaud et al. 2010) outside of cluster cores where the effects of non-gravitational physics are small. When integrated, the self-similar ICM quantities can serve as robust observational proxies for cluster mass, such as its thermal energy content, Y_X (Kravtsov et al. 2006), or its X-ray luminosity, L_X (Maughan 2007). The outer regions of clusters are ideal for robust ICM measurements and inferences of cluster mass since these measurements at large radii are less susceptible to complex astrophysical processes that affect measurements in the cluster core, such as gas cooling, star formation, and energy injections from supernovae and active galactic nuclei.

Both X-ray and SZ observations have recently measured properties of the ICM out to the virial radius (see, e.g., Reiprich et al. 2013, for review). However, some of these observations revealed several unexpected results that devi-

ate from theoretical predictions. First, hydrodynamical simulations predict that the entropy of the ICM should have a power law scaling with cluster-centric radius, as the entropy is set by the accretion shock of the cluster (Tozzi & Norman 2001; Voit et al. 2003). But, *Suzaku* X-ray measurements of the outer regions of clusters showed lower and flatter entropy profiles than the theoretically predicted power law, breaking the self-similar scaling (e.g., George et al. 2009; Bautz et al. 2009; Reiprich et al. 2009; Hoshino et al. 2010; Kawaharada et al. 2010; Akamatsu et al. 2011; Walker et al. 2013; Urban et al. 2014; Okabe et al. 2014). Additionally, *Suzaku* measured an enclosed gas mass fraction of the Perseus cluster that curiously exceeds the cosmic baryon fraction at large radii (Simionescu et al. 2011). In addition, *Chandra* follow-up observations of SZ-selected clusters from the South Pole Telescope survey also found signs of entropy flattening and redshift evolution of the pressure profile in the outer regions of clusters, indicating signatures of departures from self-similarity (McDonald et al. 2014, but see Eckert et al. 2013; Morandi et al. 2015).

In the prevalent Λ CDM picture of structure formation, galaxy clusters are dynamically young objects that are still growing via mergers and accretion. The outskirts of galaxy clusters can be regarded as “cosmic melting pots,” where infalling materials are being virialized. The accreting gas dissipates heat through shocks and turbulence, establishing the overall thermodynamical structures in galaxy clusters. An improved understanding of the “cosmic melting pot” will advance our ability to use clusters for precision cosmology, particularly in light of ongoing and upcoming multi-wavelength cluster surveys, including *Planck* and *eROSITA*.

A variety of astrophysical processes in cluster outskirts can

contribute to the observed deviations from self-similar predictions. Previous theoretical works indicated that processes such as gas inhomogeneities (Nagai & Lau 2011; Zhuravleva et al. 2013; Vazza et al. 2013; Roncarelli et al. 2013; Rasia et al. 2014) and non-thermal pressure support (e.g. Nelson et al. 2014a; Shi & Komatsu 2014; Shi et al. 2015) may play significant roles. These non-equilibrium processes are likely to be driven by mass accretion in the outskirts of clusters.

Recent N -body simulations suggested that dark matter (DM) halos accrete mass at different rates depending on their mass, redshift (e.g., Cuesta et al. 2008; McBride et al. 2009). Variations in the mass accretion rate (MAR) of halos introduce differences in the DM density profiles in halo outskirts, leading to apparent deviations from self-similarity (Diemer & Kravtsov 2014). If gas traces DM, we would expect mass accretion to similarly affect the gas distribution in cluster outskirts. Understanding the effects of MAR on gas properties in cluster outskirts requires cosmological hydrodynamic simulations that self-consistently follow the dynamics of DM and gas.

In this work, we analyze a mass-limited sample of galaxy clusters extracted from the *Omega500* cosmological hydrodynamic simulation (Nelson et al. 2014b). We find that the ICM profiles in cluster outskirts are affected by the mass accretion in two ways. First, the outer ICM profiles are more self-similar with redshift when they are normalized using the mean mass density of the universe, because the mean density traces the redshift evolution of MAR better than the critical density. Second, at any given redshift, the outer ICM profiles and the location of accretion shock around clusters are sensitive to the MAR. We also find the collisional gas does not trace accretion of the collisionless DM perfectly, leading to departures in the density ratio between gas and DM from the cosmic mean value. We discuss implications of our results on X-ray and SZ observations of the ICM profiles in cluster outskirts, mass-observable scaling relations, and the use of galaxy clusters as cosmological probes.

The paper is organized as follows. In Section 2 we describe the concepts of cluster mass definitions, self-similar model, and MAR. In Section 3 we describe our simulated cluster sample. In Section 4 we examine the dependence of the gas profiles on the definition of cluster mass and their MAR. We provide our discussion and conclusions in Section 5.

2. THEORETICAL CONSIDERATIONS

2.1. Cluster Mass Definitions

Galaxy cluster forms at the intersections of large-scale filamentary structures in the universe and they do not have well-defined physical edge. To calculate cluster masses, the common approach is to define the boundary of a cluster as a sphere enclosing an average matter density equal to a reference overdensity Δ times a reference background density, ρ_{ref} . The mass of the cluster is then given as,

$$M_{\Delta} \equiv \frac{4\pi}{3} \Delta \rho_{\text{ref}}(z) R_{\Delta}^3 \quad (1)$$

where R_{Δ} is the radius within which we compute the enclosed mass. Two common choices of the background density ρ_{ref} are the critical density, $\rho_c(z) \equiv 3H_0^2 E^2(z)/(8\pi G)$, and the mean matter density, $\rho_m(z) = \rho_c(z)\Omega_m(z)$, in the standard Λ CDM spatially flat cosmological model, where $E^2(z) \equiv \Omega_m(1+z)^3 + \Omega_{\Lambda}$, $\Omega_m(z) = \Omega_m(1+z)^3/E^2(z)$, and Ω_m (without the explicit z -dependence) refers to the present-day mass density fraction of the universe. The reference overdensity Δ is

usually chosen to be a value close to $18\pi^2 \approx 178$, which corresponds to the virial overdensity in the flat matter dominated, Einstein-de Sitter universe ($\Omega_m = 1 - \Omega_{\Lambda} = 1$). In the more realistic flat Λ CDM model, the virial overdensity varies with redshift (e.g., Bryan & Norman 1998).

In the literature, $\rho_c(z)$ has been widely used to define cluster masses ($\rho_{\text{ref}} = \rho_c(z)$, with $\Delta = \Delta_c$). In particular, $\Delta_c = 500$ has been used in the analyses of *Chandra* and *XMM-Newton* X-ray observations of galaxy clusters, since it corresponds to the radius out to which gas density and temperature profiles of the ICM can be reliably measured. $\Delta_c = 200$ is also adopted in recent *Suzaku* X-ray and *Planck* SZ observations which extended the measurements of the ICM profiles to larger cluster-centric radii. On the other hand, $\rho_m(z) \propto (1+z)^3$ is independent of other cosmological parameters, e.g., the Hubble parameter. Using $\rho_m(z)$ to define DM halos also leads to a more ‘‘universal’’ mass function (e.g., White 2002) and has been used in calibrating halo mass functions in N -body simulations (e.g., Jenkins et al. 2001; Tinker et al. 2008).

2.2. Self-similarity

In the current hierarchical structure formation model, galaxy cluster of mass M at redshift z forms from gravitational collapse of the primordial cosmological density perturbation, when its linear density fluctuation $\delta(M, z)$ reaches the collapse threshold $\delta_c = 1.686$. Since the primordial density perturbations are well-characterized by the Gaussian distribution, properties of galaxy clusters are uniquely characterized by its density peak height, $\nu(M, z) \equiv \delta_c/\sigma(M, z)$, where $\sigma(M, z)$ is the characteristic linear density fluctuation smoothed over mass scale M at redshift z .

Strictly speaking, self-similarity only holds when the initial linear density fluctuations and their subsequent gravitational collapse into cluster halos are scale-free, and there is no physical scale associated with non-gravitational processes operating during cluster formation. These conditions are approximately true for cluster-size halos, where linear density fluctuations follow a power law. During the subsequent collapse until $z \gtrsim 0.5$, the effects of dark energy are also assumed to be small, keeping cluster growth almost scale-free. Baryonic physics, such as radiative cooling, star formation and feedback, break self-similarity, but their effects are mostly confined to within the cluster core.

On large scales, the majority of the baryonic component is in the form of X-ray emitting ICM and is expected to follow the distribution of the gravitationally dominant DM. The self-similar model predicts that cluster gas profiles for a given mass (or peak height) appear ‘‘universal’’ when they are scaled with respect to the reference background density of the universe (see, e.g., Voit 2005). For example, the gas density is scaled using the mean cosmic baryon overdensity, defined as $\rho_{\text{gas},\Delta} \equiv f_b \Delta \rho_{\text{ref}}(z)$, where Δ is the redshift independent chosen overdensity, $\rho_{\text{ref}}(z)$ is the reference mass density of the universe at redshift z , and $f_b \equiv \Omega_b/\Omega_m$ is the cosmic baryon fraction. Similarly, other quantities, such as temperature, pressure, entropy, and velocity, can be normalized with appropriate scaling that depends on mass and redshift: $k_B T_{\Delta} \equiv GM_{\Delta} \mu m_p / (2R_{\Delta})$, $P_{\Delta} \equiv \rho_{\text{gas},\Delta} k_B T_{\Delta} / (\mu m_p)$, $K_{\Delta} \equiv k_B T_{\Delta} / (\mu m_p \rho_{\text{gas},\Delta}^{2/5})$, and $V_{\text{circ},\Delta} \equiv \sqrt{GM_{\Delta}/R_{\Delta}}$, where G is the gravitational constant, m_p is the proton mass and k_B is the Boltzmann constant. For the cases where the reference background density is set to the critical or the mean density, we set $\Delta = \Delta_c$ or $\Delta = \Delta_m \equiv \Delta_c/\Omega_m(z)$, respectively. In this paper, we consider two cases: $\Delta_c = 200$ and $\Delta_m = 200$. The

the self-similar values of the thermodynamical quantities for $\Delta_c = 200$ are:

$$\rho_{200c} = 4.759 \times 10^{-14} E(z)^2 M_\odot \text{Mpc}^{-3}, \quad (2)$$

$$k_B T_{200c} = 8.145 \text{ keV} \left(\frac{M_{200c}}{10^{15} h^{-1} M_\odot} \right)^{2/3} E(z)^{2/3}, \quad (3)$$

$$P_{200c} = 2.660 \times 10^{-3} \text{ keV cm}^{-3} \left(\frac{M_{200c}}{10^{15} h^{-1} M_\odot} \right)^{2/3} E(z)^{8/3}, \quad (4)$$

$$K_{200c} = 1718 \text{ keV cm}^2 \left(\frac{M_{200c}}{10^{15} h^{-1} M_\odot} \right)^{2/3} E(z)^{-2/3}; \quad (5)$$

and for $\Delta_m = 200$:

$$\rho_{200m} = 1.285 \times 10^{-12} (1+z)^3 M_\odot \text{Mpc}^{-3}, \quad (6)$$

$$k_B T_{200m} = 5.265 \text{ keV} \left(\frac{M_{200m}}{10^{15} h^{-1} M_\odot} \right)^{2/3} (1+z), \quad (7)$$

$$P_{200m} = 4.641 \times 10^{-4} \text{ keV cm}^{-3} \left(\frac{M_{200m}}{10^{15} h^{-1} M_\odot} \right)^{2/3} (1+z)^4, \quad (8)$$

$$K_{200m} = 2800 \text{ keV cm}^2 \left(\frac{M_{200m}}{10^{15} h^{-1} M_\odot} \right)^{2/3} (1+z)^{-1}. \quad (9)$$

We adopt $f_b = 0.1737$ from the *WMAP5* cosmology used in this work, and $\mu = 0.59$ to be the mean particle weight of the fully ionized ICM.

2.3. Mass Accretion Rate (MAR)

In this work, we propose a proxy for the *instantaneous* MAR α_Δ , defined as the ratio of radial infall velocity to the circular velocity of the cluster halo measured at some chosen radius R_α ,

$$\alpha_\Delta = \frac{V_r^{\text{DM}}(r = R_\alpha)}{V_{\text{circ},\Delta}}, \quad (10)$$

where R_α is a free parameter denoting a certain radius located inside the infall region where $V_r^{\text{DM}} < 0$. Physically, a halo that is actively accreting in its outskirts will have a large negative value of α_Δ .

Diemer & Kravtsov (2014) proposed a different MAR proxy Γ_Δ :

$$\Gamma_\Delta = \frac{\log_{10}(M_\Delta(a_0)/M_\Delta(a_1))}{\log_{10}(a_0/a_1)} \quad (11)$$

where $M_\Delta(a_0)$ and $M_\Delta(a_1)$ are the mass of the halo at $a_0 = 1$ ($z = 0$) and its progenitor at $a_1 = 0.67$ ($z = 0.5$) respectively. A higher Γ_Δ means that the halo has experienced a greater *physical* mass accretion between the two redshifts.

Our proposed MAR proxy α_Δ have an advantage over Γ_Δ because α_Δ can be measured for halos at any given redshift, while Γ_Δ is an integrated quantity defined between two chosen redshifts. α_Δ is also in principle an observable quantity that can be measured from radial velocities of infalling galaxies or gas in cluster outskirts. We compare these two MAR proxies in Section 4.3.

3. COSMOLOGICAL HYDRODYNAMIC SIMULATIONS

3.1. Data and Halo Selection

In this work we analyze a sample of simulated galaxy clusters from the *Omega500* Simulation Project (Nelson et al. 2014b), which is a high-resolution hydrodynamical simulation of a large cosmological volume with the comoving box length of $500 h^{-1} \text{Mpc}$. The simulation is performed using the Adaptive Refinement Tree (ART) *N*-body+gas-dynamics code (Kravtsov 1999; Kravtsov et al. 2002; Rudd et al. 2008), which is an Eulerian code that uses adaptive refinement in space and time, and non-adaptive refinement in mass (Klypin et al. 2001) to achieve the dynamic ranges to resolve the cores of halos formed in self-consistent cosmological simulations in a flat Λ CDM model with WMAP 5 years (*WMAP5*) cosmological parameters: $\Omega_m = 1 - \Omega_\Lambda = 0.27$, $\Omega_b = 0.0469$, $h = 0.7$ and $\sigma_8 = 0.82$, where the Hubble constant is defined as $100 h \text{ km s}^{-1} \text{Mpc}^{-1}$ and σ_8 is the mass variance within spheres of radius $8 h^{-1} \text{Mpc}$. The simulation is performed on a uniform 512^3 grid with 8 levels of mesh refinement, implying a maximum comoving spatial resolution of $3.8 h^{-1} \text{kpc}$. Our simulations are based on simple non-radiative hydrodynamics, allowing us to isolate the effects of MAR on self-similarity from the effects of complicated galaxy formation physics, which are expected to be small in the outskirts of clusters. The current work also serves as a baseline for future studies of the effects of such physics.

Galaxy clusters are identified in the simulation using a spherical overdensity halo finder described in Nelson et al. (2014b). We select clusters with $M_{500c} \geq 3 \times 10^{14} h^{-1} M_\odot$ at $z = 0$ and re-simulate the box with higher resolution DM particles in regions of the selected clusters, resulting in an effective mass resolution of 2048^3 , which corresponds to a mass resolution of $1.09 \times 10^9 h^{-1} M_\odot$. To study the redshift evolution for the ICM profiles, we extract halos from four redshift outputs: $z = 0.0, 0.5, 1.0, 1.5$. At each redshift we apply a mass cut to ensure a mass-limited sample by comparing our mass function to that of Tinker et al. (2008) and setting the mass cut to ensure that the sample is complete above the chosen mass threshold. The mass-cuts and resulting sample sizes are as follows: 65 clusters with $M_{200m} \geq 6 \times 10^{14} h^{-1} M_\odot$ at $z = 0$, 48 clusters with $M_{200m} \geq 2.5 \times 10^{14} h^{-1} M_\odot$ at $z = 0.5$, 42 clusters with $M_{200m} \geq 1.3 \times 10^{14} h^{-1} M_\odot$ at $z = 1.0$, and 42 clusters with $M_{200m} \geq 7 \times 10^{13} h^{-1} M_\odot$ at $z = 1.5$.

3.2. Substructure Removal and Profile Making

In this work we are primarily interested in the thermodynamic properties of the diffuse ICM. Gas in dense clumps and filaments is expected to have different thermodynamical properties from the diffuse ICM. In this work we minimize their effects by identifying and removing these gaseous substructures directly in simulations. Using the method proposed by Zhuravleva et al. (2013), we remove gas clumps by excluding gas cells that have logarithmic density 3.5σ above the median for a given radial bin. Similarly we remove gaseous filamentary structures by excluding radially infalling gas cells with logarithmic density between 1σ and 3.5σ above the median for a given radial bin. As shown in Figure 1, this method can identify gas associated with clumps and filaments in the cluster outskirts quite well.

After removing clumps and filaments, we compute the spherically averaged profiles by dividing the analysis region for each cluster into 99 spherical logarithmically spaced bins from $10 h^{-1} \text{kpc}$ to $10 h^{-1} \text{Mpc}$ (comoving) in the radial direction from the cluster center, which is defined as the position with the maximum binding energy. Our results are insensitive to the exact choice of binning. We then compute volume-

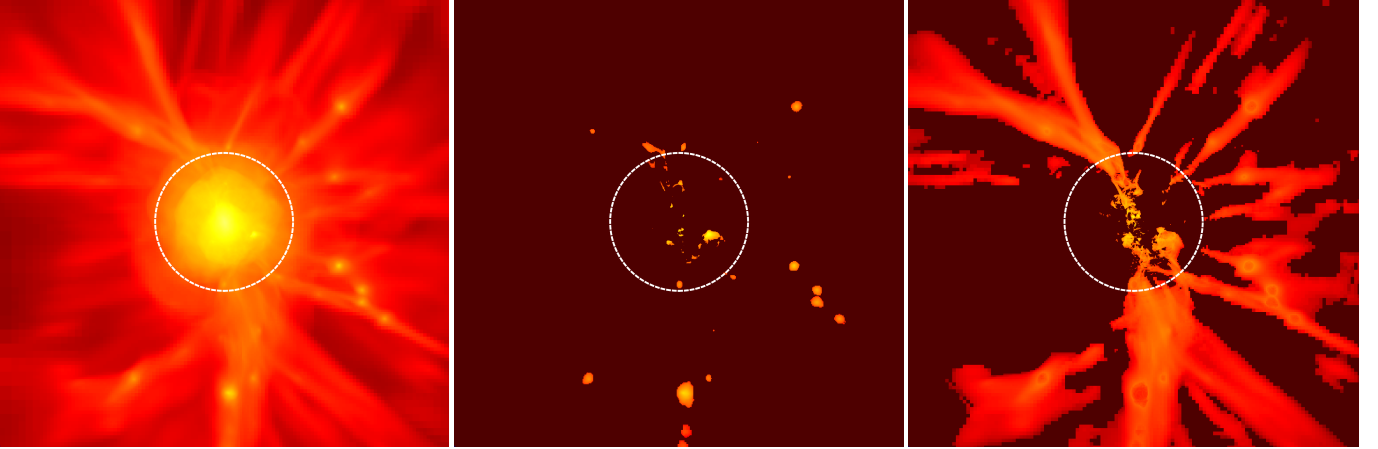


Figure 1. Projected gas density maps of one of the $z = 0$ clusters selected from the sample. From left to right: map of the total gas, clumps, and filaments. The dimension for each panel is $15.6 h^{-1} \text{Mpc} \times 15.6 h^{-1} \text{Mpc}$, with depth of $1.9 h^{-1} \text{Mpc}$. The circle in dashed line shows $R_{200m} = 3.3 h^{-1} \text{Mpc}$ of the cluster.

weighted mean profiles of density, pressure, and entropy, and mass-weighted mean profiles of gas temperature and gas velocities for each cluster halo, and present their mean profiles averaged over the cluster sample. For the rest of the paper, all of the gas profiles are presented with substructures and filaments removed, unless noted otherwise.

4. RESULTS

4.1. Self-similarity of Gas Profiles

We begin by comparing radial velocity profiles of gas and DM in clusters defined with respect to the critical density and the mean density of the universe. The velocity profiles are normalized by the circular velocity $V_{\text{circ},\Delta} \equiv \sqrt{GM_{\Delta}/R_{\Delta}}$. In Figure 2 we show the evolution of radial velocities for gas between $z = 1.5$ and $z = 0.0$. The top left panel shows the profiles for clusters normalized by using $\Delta_c = 200$, and the top right panel shows the profiles of the same clusters normalized by using $\Delta_m = 200$. For $\Delta_c = 200$, there is significant redshift evolution in the radial gas velocity profile, where $V_r(r = R_{200c})$ varies from $-0.3V_{200c}$ to ≈ 0 from $z = 1.5$ to $z = 0$. Outside R_{200c} , the radial velocities of DM and gas are mostly negative, indicating infall of DM and gas onto the cluster halos. The magnitude of the velocities in these infall regions evolves with redshift: higher- z clusters show more negative radial velocities, indicating their higher MAR. The location of the velocity minimum, where the gas is infalling most strongly, also evolves with z , and it is located at larger fraction of R_{200c} at lower z . In the same figures, we also show the average radial velocities of DM (indicated by the dashed lines). Although the radial velocity profiles of both gas and DM show similar qualitative trend with z , gas is generally accreting at a slower rate than DM; the collisional gas¹ experiences ram pressure from the surrounding ICM, while the collisionless DM does not.

At large radii ($r \gtrsim 3R_{200c}$), gas traces DM, where the velocities of both components follow the Hubble flow in the expanding universe. Their normalized radial velocity profiles are independent of redshift, because the normalization with

¹ Note that the mean free path of electrons in the ICM plasma could be large ($\gtrsim 100 \text{kpc}$), which may break down the hydrodynamic approximation in cluster outskirts. However, the presence of any magnetic field may reduce the effective mean free path below the numerical resolution such that the ICM can be treated effectively as collisional. This uncertainty must be kept in mind when interpreting our results.

respect to R_{200c} and $V_{\text{circ},200c}$ naturally accounts for the Hubble flow: $R_{200c} \propto \rho_c^{-1/3} \propto H(z)^{-2/3}$, and $V_{\text{circ},200c} \propto H(z)^{1/3}$, so $H(z) = V_r/r \propto V_{\text{circ},200c}/R_{200c}$, leaving the normalized radially velocity profile $V_r(r/R_{200c})/V_{\text{circ},200c}$ redshift independent.

An interesting radius is the turnaround radius R_{ta} , where the radial velocity becomes zero as the accreting mass detaches from the Hubble flow. The top left panel of Figure 2 shows that R_{ta}/R_{200c} (the outermost radius where the radial velocity is zero) is independent of redshift, and it is located at $R_{\text{ta}}/R_{200c} \approx 5$. We expect R_{ta} to follow the evolution of the Hubble parameter, as it is the radius where the dynamics of both dark matter and gas detach from the Hubble flow. Therefore R_{ta} is well-traced by R_{200c} which is defined in terms of the Hubble parameter.

On the other hand, R_{ta} does not scale well with R_{200m} . The radial velocity profiles $V_r/V_{\text{circ},200m}$ outside the infall region show strong evolution with z , especially at late times ($z \lesssim 1.0$). This is because $R_{200m} \propto \rho_m(z)^{-1/3}$ only accounts for the evolution of the matter component, but does not account for the effects of dark energy which drives the accelerated expansion of the universe at low z , leading to strong evolution trend in R_{ta}/R_{200m} and the radial velocity profile outside the infall region.

However, at smaller radii, we find that choosing $\Delta_m = 200$ makes the radial velocity profile more universal with z . The locations of radial velocity minima in both DM and gas for $\Delta_m = 200$ show little redshift evolution compared to the case of $\Delta_c = 200$. This behavior is expected, as the accreting matter undergoes free-fall once decoupled from the Hubble flow, where its evolution is governed primarily by the gravity inside the virialized region, whose mass density is characterized by the cosmic mean mass density independent of the Hubble parameter.

Similar trends are observed in the entropy profiles of gas. The profiles are normalized by the self-similar values described in the Section 2.2. The bottom panels of Figure 2 show the redshift evolution of the entropy profiles. Each line represents the entropy profile averaged over the cluster sample at $z = 0.0, 0.5, 1.0, 1.5$. Each profile shows a well-defined entropy peak, which corresponds to the location of the accretion shock², R_{sh} , where the gas radial velocity is minimum.

² We define accretion shocks as regions where pristine gas from voids falls into the cluster and gets shock-heated for the first time, which are commonly referred to as “external” shocks, in contrast to “internal” shocks driven by

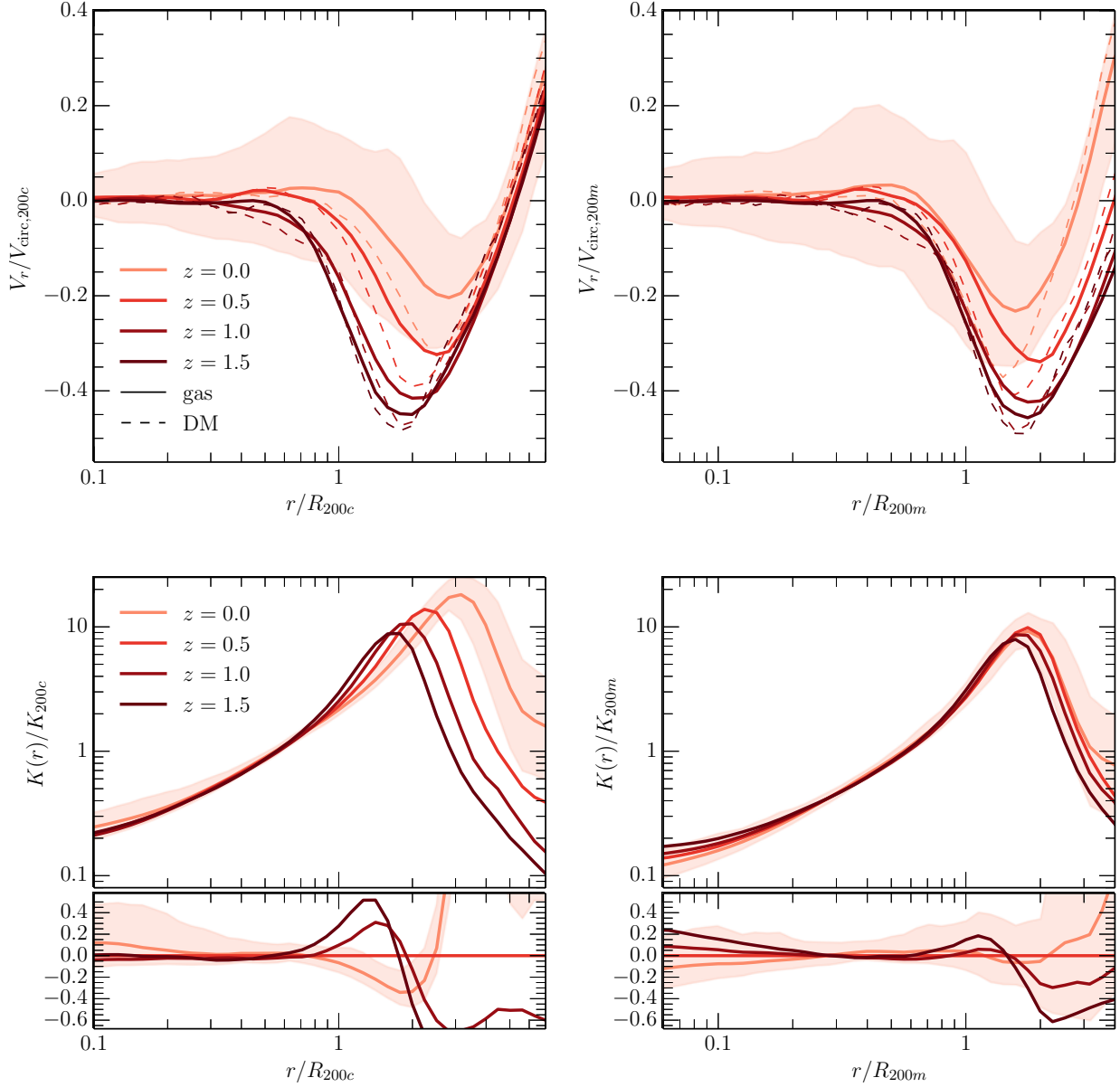


Figure 2. Profiles of average radial velocity (*top panels*) and gas entropy (*bottom panels*) at $z=0, 0.5, 1.0,$ and 1.5 . The lower subplot in each panel shows the deviations of the profiles from different z outputs relative to that of the $z=0.5$ clusters. The *left* panels show the profiles of cluster halos defined using the critical density, while the *right* panels show the profiles of the same cluster halos defined using the mean density. In the upper panel, we show the *mean* radial velocity profiles for gas and DM in *solid* and *dashed* lines respectively. The shaded regions indicate the 1σ scatter around the mean gas profiles for the $z=0$ clusters.

Some care is needed when interpreting the accretion shock radius R_{sh} defined using the entropy peak or the minimum of the radial infall velocity of gas. When the accreting collisional gas is shocked, it stops infalling and its radial velocity should jump abruptly to zero. Likewise, the gas entropy profile should jump sharply behind the accretion shock when the gas is heated through the shock. However, these sharp jumps are not seen in our radial velocity nor entropy profiles, which increase more smoothly in the post-shock region. This is partly because gas accretion is aspherical, and the actual topology of the accretion shocks is rather complex (e.g., Ryu et al. 2003; Pfrommer et al. 2006; Skillman et al.

2008; Vazza et al. 2009a; Planelles & Quilis 2013; Schaal & Springel 2015). Spherically averaging the velocity and entropy profiles will smooth out these jumps. Moreover, cold gas accreting along filaments can penetrate deeper into the cluster and are shocked at smaller cluster-centric radii (e.g., Molnar et al. 2009). This creates a series of shocks with varying velocity and entropy jumps, smoothing the velocity and entropy profiles in the infall region.

For $\Delta_c = 200$, the accretion shock systematically increases toward larger cluster-centric radii at lower z . The entropy measured at $r = R_{200c}$ decreases from $3 \times K_{200c}$ at $z = 1.5$ to $1.5 \times K_{200c}$ at $z = 0$ due to the combination of the shift in the location of the entropy peak and the evolution in the entropy normalization K_{200c} . On the other hand, for $\Delta_m = 200$, the

mergers or accretions through filaments (e.g., Ryu et al. 2003).

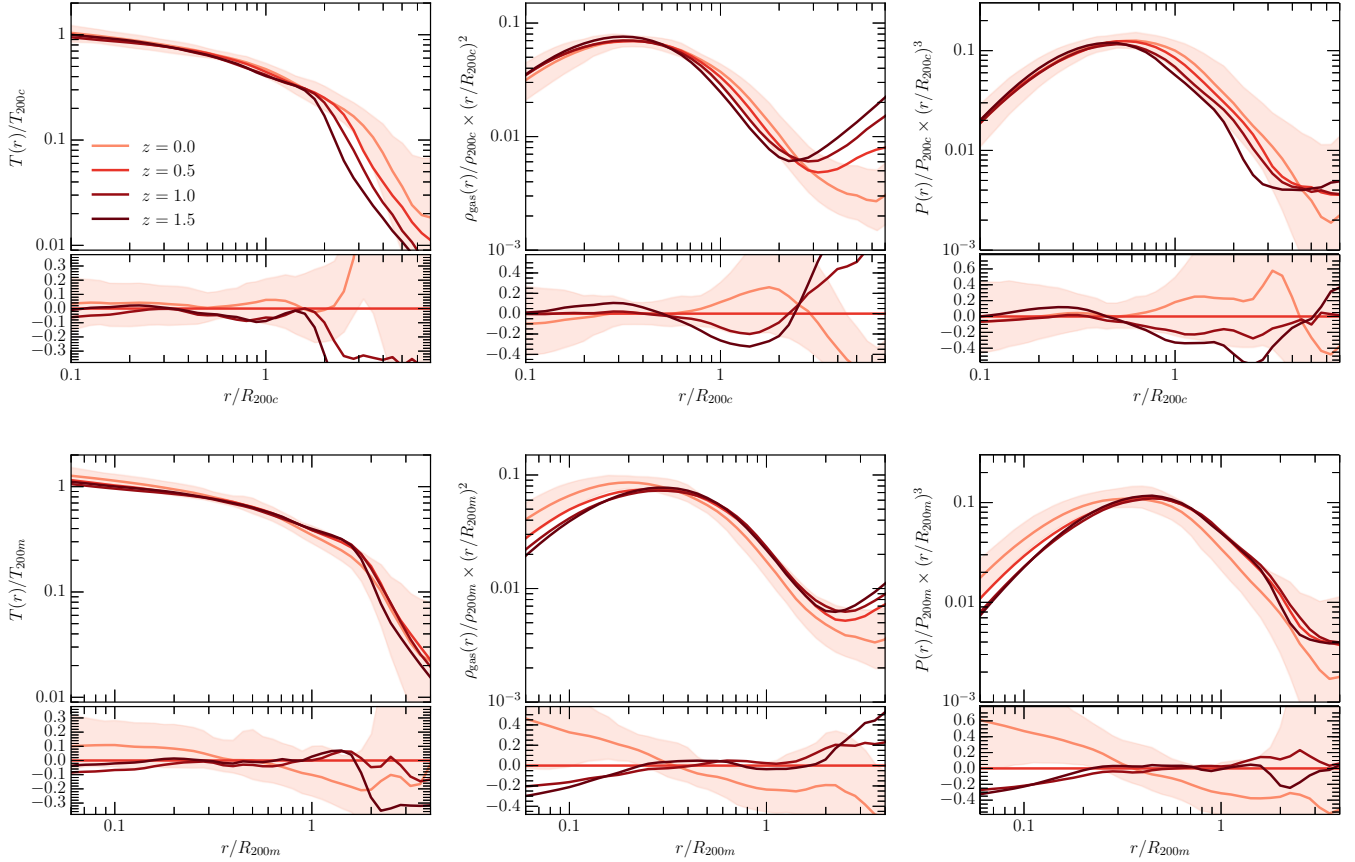


Figure 3. From left to right, we show the profiles of gas temperature, density, and pressure for the cluster halos at $z = 0.0, 0.5, 1.0, 1.5$. The upper panels show the profiles normalized using the critical density $200 \times \rho_c(z)$, while the lower panels show the same profiles normalized using the mean density $200 \times \rho_m(z)$. In each figure, the bottom sub-panel shows the fractional deviations of the profiles with respect to the $z = 0.5$ clusters. The shaded regions indicate the 1σ scatter around the mean for the $z = 0$ clusters.

entropy profiles in the radial range of $0.3 \leq r/R_{200m} \leq 1.0$ remain roughly constant with z . The accretion shock radius R_{sh}/R_{200m} does not evolve much, and it is located at $R_{\text{sh}} \approx 1.6R_{200m}$ at all z .

In Figure 3, we show profiles of other thermodynamic quantities: gas density, temperature and thermal pressure profiles normalized using $\Delta_c = 200$ and $\Delta_m = 200$ at different z . We find that these ICM profiles exhibit similar z -dependence to that of the entropy profile. For $\Delta_c = 200$, there are systematic deviations of the profiles with z outside the cluster core ($r \geq 0.2R_{200c}$). For example at $r = R_{200c}$, high- z clusters have lower normalized temperature because they have higher physical mass accretion rate, so that their accretion shocks can penetrate deeper by pushing the low-temperature pre-shock regions toward the inner regions of clusters. Similarly, the evolution in the normalized density and pressure profiles is also due to the evolution in R_{sh}/R_{200c} . On the other hand, switching the halo definition to $\Delta_m = 200$ captures the redshift evolution of the R_{sh} much better and results in thermodynamic profiles that are more universal with z in the radial range of $0.3 \leq r/R_{200m} \leq 1.0$.

The self-similar secondary infall model predicts that the location of shock is located at a fixed fraction of the current turnaround radius, with $R_{\text{sh}} = 0.347R_{\text{ta}}$, in the flat matter-dominated universe (Bertschinger 1985). However, our simulation shows that R_{sh} is *not* proportional to R_{ta} . R_{sh} evolves as R_{200m} , whereas R_{ta} evolves as R_{200c} . This deviation from

the self-similar secondary infall model is likely due to the increasing effects of dark energy at low z , which breaks the self-similar evolution of infalling matter that is currently turning around. We will investigate the origin of this deviation in a future paper.

We find little dependence of the gas profiles on cluster mass or density peak height $\nu \equiv \delta_c/\sigma(M, z)$ defined in Section 2.2, because our sample contains only massive clusters. On average, halos with higher mass or peak height are on average accreting more rapidly compared to those with low mass or peak height (Cuesta et al. 2008; McBride et al. 2009; Diemer & Kravtsov 2014), which can introduce mass or peak height dependence in the outskirts gas profiles.

Baryonic processes such as radiative cooling, star formation, and energy feedback from supernovae or active galactic nuclei can significantly influence the gas profiles in the inner regions and break self-similar behavior. These physical processes can also change the thermodynamical structure at larger radii and influence gas dynamics in low mass halos, such as galaxies and galaxy groups (e.g., Faucher-Giguère et al. 2011; van de Voort et al. 2011). We expect the effects of baryonic physics to be considerably smaller in the outskirts of massive halos, where gravitational physics dominates the gas dynamics. However, further work is necessary to fully quantify how baryons affect the MAR and the self-similarity of gas profiles in all halos. A study of gas flows in group and galaxy-size halos help address these issues (e.g., Wetzel

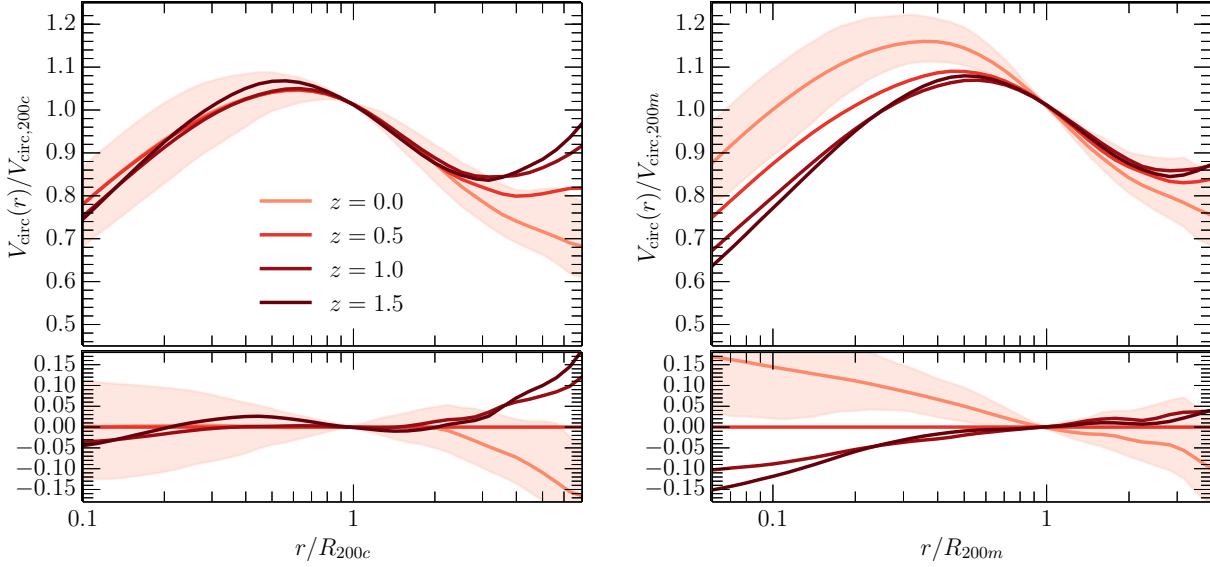


Figure 4. Profiles of circular velocity $V_{\text{circ}} \equiv \sqrt{GM(<r)}/r$ at $z=0.0, 0.5, 1.0, 1.5$. The *left* panel shows the profiles of the cluster halos defined using the critical density, while the *right* panel shows the same profiles with cluster halos defined using the mean density. In each figure, the bottom sub-panel shows the fractional deviations of the profiles with respect to the profile of the $z=0.5$ clusters. The shaded regions indicate the 1σ scatter around the mean for the $z=0$ clusters.

& Nagai 2014).

4.2. Evolution of the Circular Velocity Profile

The differences in the self-similarity between the inner and outer regions can be understood in terms of the evolution of the gravitational potential well, which determines the thermodynamical properties of the cluster gas. In Figure 4, we plot the circular velocity profile $V_{\text{circ}}(r)$ which we use as a proxy for the gravitational potential, normalized using $\Delta_c = 200$ and $\Delta_m = 200$ at $z=0.0, 0.5, 1.0, 1.5$. For $\Delta_c = 200$, the circular velocity profile is more universal with z at $r \leq R_{200c}$, indicating that the evolution of the cluster potential in the inner region is well captured by $\rho_c(z)$. On the other hand for $\Delta_m = 200$, V_{circ} evolves significantly at $r \leq R_{200m}$, but exhibits an enhanced level of self-similarity at $r \geq R_{200m}$.

The reason behind the dependence is that the gravitational potential well of the cluster halo is already set during the early stage of formation of the halo (Li et al. 2007; van den Bosch et al. 2014), while the outer region is more sensitive to the recent mass growth of the halo. N -body simulations have shown that halo grows in two phases: an early fast growth phase when the halo is formed via violent relaxation and phase mixing, followed by slow growth phase via smooth accretion (Wechsler et al. 2002; Zhao et al. 2003). The initial fast growth phase determines the inner density and hence the potential well of the halo. For a massive cluster-size halo at $z=0$, its fast growth phase occurs at high redshift ($z \gtrsim 1$) when the universe is still flat and matter-dominated, with its gravitational potential forming and scaling with the background density where $\rho_m(z) = \rho_c(z)$. During the subsequent slow growth phase in the epoch of dark energy domination ($\rho_m(z) < \rho_c(z)$), accretion only adds mass in the halo outskirts, leaving the inner mass distribution unchanged. For constant mass, the radius defined with respect to the critical density scales as $R_{\Delta_c} \propto \rho_c(z)^{-1/3} \propto E(z)^{-2/3}$, which evolves much slower than $R_{\Delta_m} \propto (1+z)^{-1}$ at late times when the universe is no longer matter-dominated. Therefore, R_{Δ_c} tracks the slowly changing

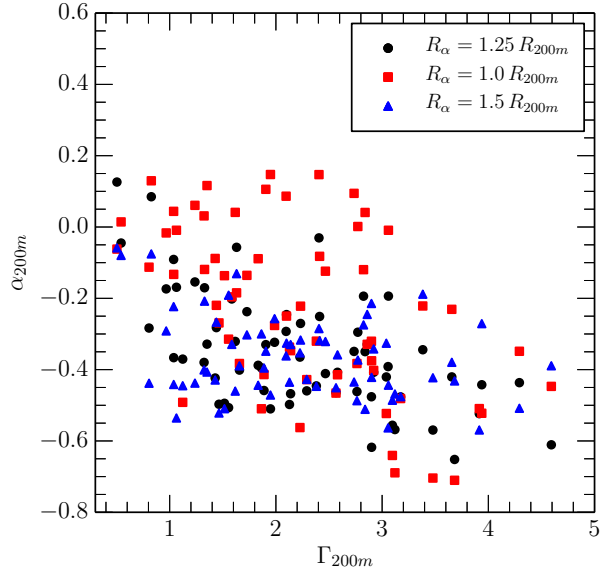


Figure 5. Comparison between two MAR proxies α_{200m} versus Γ_{200m} for the $z=0$ clusters. Here, we consider three values of α_{200m} based on the DM radial velocity at $r = 1.25R_{200m}$ (black circles), $1.0R_{200m}$ (red squares), and $1.5R_{200m}$ (blue triangles), normalized by the circular velocity at $r = R_{200m}$.

interior better, while R_{Δ_m} tracks the outer gas profiles determined by the mass accretion at late times. Further works are needed to understand the tight self-similar scaling of the inner profiles with $\rho_c(z)$. However, we note that in reality, the inner profiles are modified by baryonic physics which breaks the self-similarity (e.g., McDonald et al. 2014).

4.3. Effects of MAR on Gas Profiles

Next we study the dependence of the gas profiles on the MAR in the present-day universe at $z=0$. We use the MAR

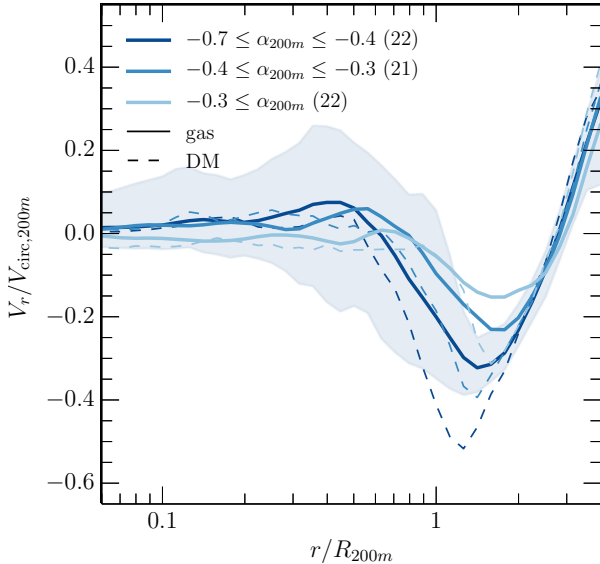


Figure 6. Profiles of radial velocity of DM (*dashed* lines) and gas (*solid* lines) in different bins of MAR α_{200m} for the $z=0$ clusters. The shaded regions represent 1σ scatter in the profiles with the most negative α_{200m} . The scatter for the other α_{200m} bins are similar in size. The numbers in the parentheses indicate the number of clusters in each α_{200m} bin.

proxy α defined in Equation 10 as a probe the MAR of the cluster. We choose $\Delta_m = 200$ to define α since it scales out the redshift dependence of the MAR, as shown in Section 4.1.

We first compare our new MAR proxy α_{200m} , based on DM infall velocities defined in Equation 10, with Γ_{200m} given by Equation 11. In Figure 5, we plot α_{200m} as a function of Γ_{200m} , with $R_\alpha/R_{200m} = 1.0, 1.25$, and 1.5 . There is a clear anti-correlation between Γ_{200m} and α_{200m} for the above values of R_α/R_{200m} , suggesting that the instantaneous MAR proxy α_{200m} is a good alternative probe of Γ_{200m} . In particular, we find that setting $R_\alpha = 1.25R_{200m}$ minimizes the scatter in $\alpha_{200m} - \Gamma_{200m}$, elucidating the clearest dependence of the thermodynamic profiles on the MAR.

Figure 6 shows the radial velocity profiles of gas and DM for clusters in three bins of α_{200m} , with each bin containing clusters that lie in the top, middle, and bottom third of the distribution in α_{200m} . Not surprisingly, rapidly accreting clusters (with more negative α_{200m}) show more negative gas radial velocity in the infall region $0.6 \lesssim r/R_{200m} \lesssim 3$. The radial gas velocity also becomes progressively less negative, with decreasing size in the infall regions for systems with a less negative α_{200m} . Note that the radial velocity of gas in the infall region is generally less negative than that of DM because the collisional gas slows down at it experiences shocks and ram-pressure of the surrounding ICM. Note, although we treat the DM and gas flows as spherical mass shells moving radially, in reality they are likely to occur anisotropically through mergers and accretions along filaments.

In Figure 7 we plot the profiles of entropy, temperature, and pressure for the three different bins of α_{200m} . The left panel of the figure shows the entropy profile. The peak of the entropy profile indicates the accretion shock radius R_{sh} , which shifts toward the inner regions for higher MAR clusters. This is because more rapidly accreting halos accumulate gas with higher momentum flux, which penetrates deeper into the interior region (e.g., Voit et al. 2003; McCourt et al. 2013) and

shifting the entropy peak and the entropy profile inward. We note that low MAR clusters do not show flatter entropy profile. This is at odds with the model put forward by Cavaliere et al. (2011), who suggested that the flattening of entropy in cluster outskirts revealed by *Suzaku* (e.g., Simionescu et al. 2011; Walker et al. 2013) may be due to weakening of accretion shocks as MAR drops due to the repulsive of dark energy at late cosmic time. Our simulation shows the opposite. The maximum entropy values of the low MAR clusters are slightly higher than, but still consistent with those of the high MAR clusters. There is a relatively modest $< 20\%$ drop in entropy at $\lesssim R_{200m}$ in the low MAR clusters due to the outward shift of the entropy profile toward larger radii compared to high MAR clusters. This small entropy drop is not enough to explain the observed entropy flattening in *Suzaku*.

Other processes may be responsible for the observed flattening of the entropy profiles in the outskirts of relaxed clusters. For example, the radially dependent ICM inhomogeneities can lead to overestimates in the gas density profiles derived from X-ray observations, causing the observed entropy profile to flatten at the large cluster-centric radii (Nagai & Lau 2011). Non-thermal pressure due to gas motions induced by gas accretion and mergers (e.g., Vazza et al. 2009b; Nelson et al. 2012) as well as plasma effects (e.g., magnetothermal instability, Parrish et al. 2012) can also bias the gas temperature and entropy profiles low at large cluster-centric radii by keeping some of the gas energy non-thermal. Non-equilibrium electrons can also lower the measured electron temperature inside the accretion shock (e.g., Rudd & Nagai 2009), which might partially explain the observed entropy drop in the outskirts (Hoshino et al. 2010; Akamatsu et al. 2011).

The average gas temperature in more rapidly accreting clusters is lower than the value of the whole cluster sample, especially in their outskirts where gas is actively accreting, but the impact of MAR on the temperature profiles is smaller within R_{200m} than the entropy profile. At $r = R_{200m}$, the most rapidly accreting clusters have temperature that is about 9% lower than the least accreting systems. The differences become larger at $r > R_{200m}$, reaching 15% at $r = 1.5R_{200m}$. The gas temperature of high MAR clusters is lower in the outskirts because their accretion shocks are located at smaller radii, and a larger fraction of the outskirts gas is still pre-shocked and has lower temperature.

Note that our results on the temperature profile and its dependence on MAR are qualitatively different from results based on idealized simulations by McCourt et al. (2013), who reported that clusters with higher accretion rates have higher temperatures than slowly accreting systems. The discrepancy could be due to their assumption of instantaneous thermalization of accreting gas at the accretion shocks, which could cause the gas temperature to be overestimated. Taking into account the residual kinetic energy from incomplete thermalization in the form of non-thermal pressure could account for this problem. High MAR clusters are expected to have a higher non-thermal pressure fraction due to the increased level of merger- and accretion-induced gas motions (Nelson et al. 2014a; Shi & Komatsu 2014; Shi et al. 2015). Therefore, the over-predicted gas temperature in the model of McCourt et al. (2013) can be lowered by the correspondingly larger amount of non-thermal pressure present in the high MAR clusters, which could bring their results in better agreement to the results of cosmological simulations.

On the right panel of Figure 7 we show the thermal pressure

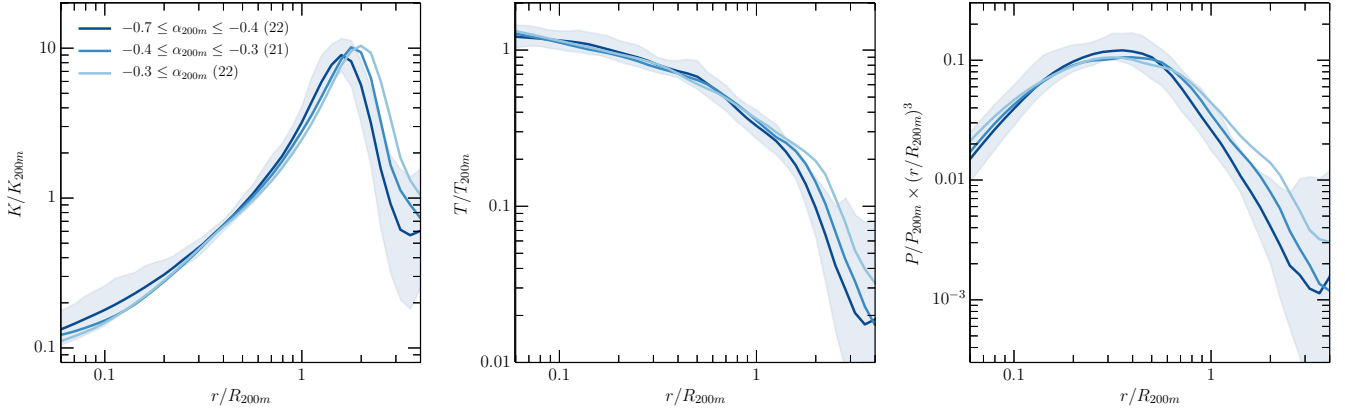


Figure 7. Profiles of gas entropy (*left*), temperature (*middle*), and pressure (*right*) scaled with R_{200m} as a function of MAR α_{200m} for the $z = 0$ clusters. We have multiplied the pressure profile by the radius cubed to show its dependence on α_{200m} more clearly. The shaded regions represent 1σ scatter in the profiles with the most negative α_{200m} . The scatter for the other α_{200m} bins are similar in size. The numbers in the parentheses indicate the number of clusters in each α_{200m} bin.

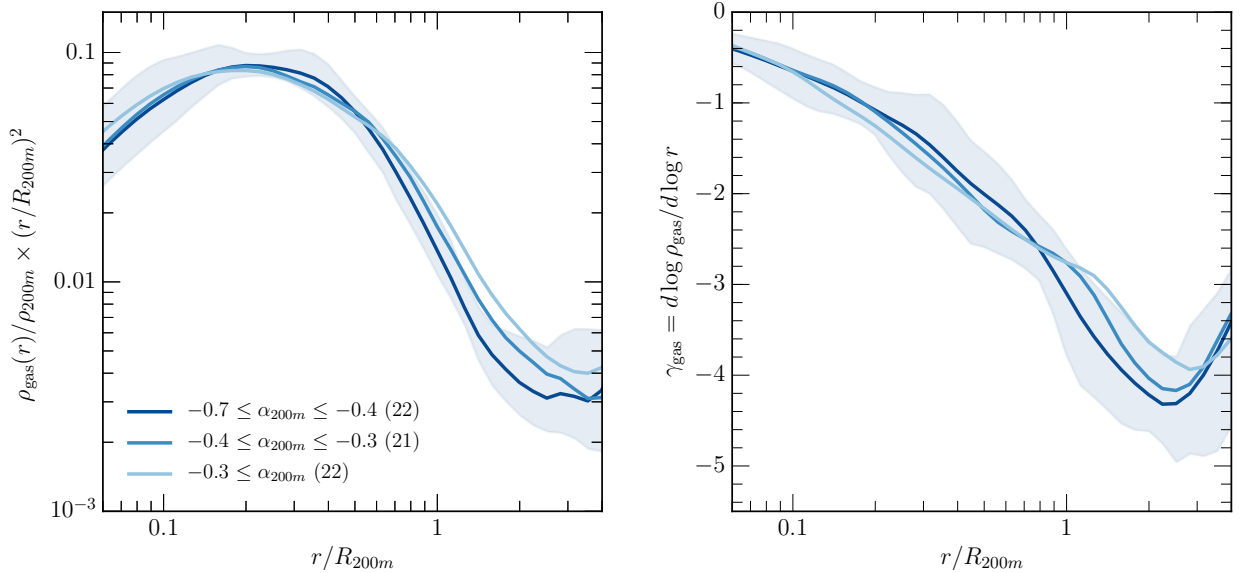


Figure 8. Profiles of gas density (*left*) and its logarithmic slope (*right*) as a function of the cluster-centric radius r/R_{200m} for different MAR α_{200m} at $z = 0$. The pressure profiles are multiplied by the square of the normalized radius to demonstrate its dependence on α_{200m} more clearly. The shaded regions represent 1σ scatter in the profile with the most negative α_{200m} . The scatter for the other α_{200m} bins are similar in size. The numbers in the parentheses indicate the number of clusters in each α_{200m} bin.

profile and its dependence on MAR. We multiply the pressure profile by the radius cubed to show more clearly the dependence on α_{200m} in the outskirts. Rapidly accreting clusters exhibit lower thermal pressure than slowly accreting systems by $\sim 40\%$, as recently accreted gas is less thermalized and less dense (see Figure 8).

The left panel of Figure 8 shows the effect of the MAR α_{200m} on gas density. We have multiplied the density profile by the radius squared to show the dependence on α_{200m} more clearly. Similar to the pressure profile, there is a factor of 2 difference in the gas density between the least and most rapidly accreting clusters at R_{200m} . The larger inflow in rapidly accreting clusters is responsible for the decrease in density at $0.5 \leq r/R_{200m} \leq 1$. The right panel of Figure 8 shows the logarithmic gas density slope $\gamma_{\text{gas}} \equiv$

$d \log \rho_{\text{gas}} / d \log r$. More rapidly accreting clusters have shallower density slopes in gas densities at $0.1 \leq r/R_{200m} \leq 0.3$ and slightly steeper slope at $0.3 \leq r/R_{200m} \leq 1$. The dependence of gas density slope on MAR or the halo formation history is consistent with that of the DM density slope seen in N -body simulations (Diemer & Kravtsov 2014; Wu et al. 2013). We note, however, that there is a large scatter in the gas density slopes for a given α_{200m} bin.

4.4. How Does Gas Trace DM in Cluster Outskirts?

In this section we examine how well gas density traces DM density in cluster outskirts and its dependence on redshift and MAR. The relation between gas and DM densities can be useful for prescribing gas distribution in DM-only simulations, or for inferring the DM distributions from the observed gas distributions in cluster outskirts. Note that in this section, we do

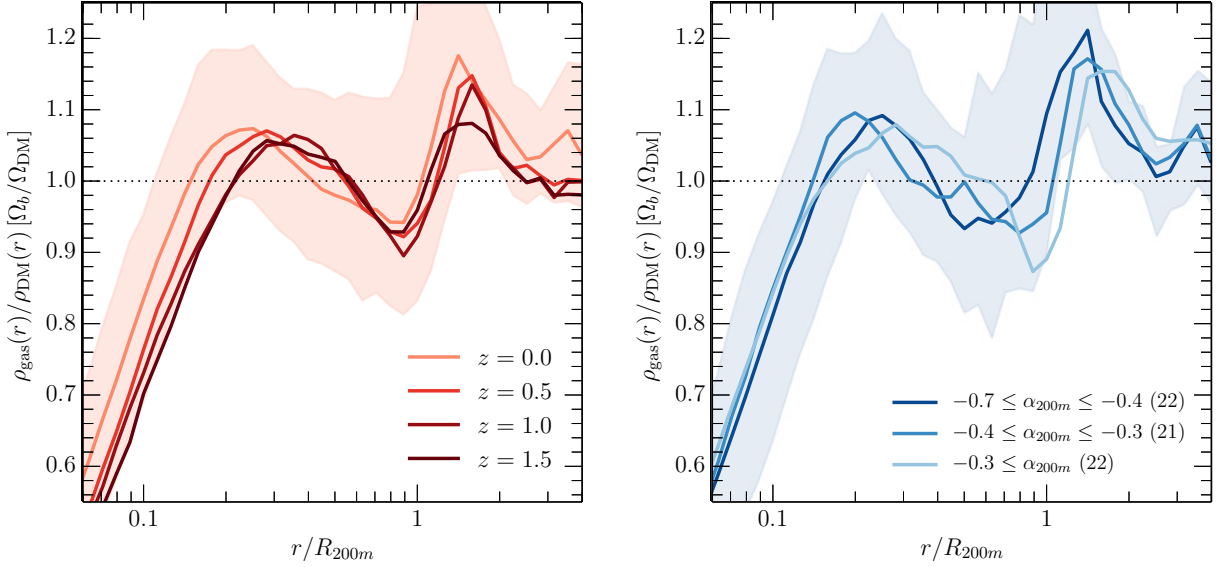


Figure 9. The ratio of mean gas density to mean DM density profile normalized by the cosmic baryon to DM density for different redshifts $z = 0, 0.5, 1.0,$ and 1.5 (left panel) and for different MAR α_{200m} at $z = 0$ (right panel). The shaded regions represent 1σ scatter in the profile for clusters at $z = 0$ (left panel) and the profile with the most negative α_{200m} (right panel). The scatter for the other z and α_{200m} bins are similar in size.

not exclude substructures and filaments in either gas or DM components.

We find that gas traces DM in a uniform manner with redshift when we define clusters with $\Delta_m = 200$. The left panel of Figure 9 shows the ratio of gas-to-DM density ($\rho_{\text{gas}}/\rho_{\text{DM}}$) as a function of the cluster-centric radius at $z = 0.0, 0.5, 1.0, 1.5$. Here, the gas and DM densities shown are the mean values in each spherical bin, and the ratio is normalized to the cosmic baryon-to-DM ratio ($\Omega_b/\Omega_{\text{DM}}$). Similar to the thermodynamic profiles discussed in Section 4.1, the profile of $\rho_{\text{gas}}/\rho_{\text{DM}}$ is universal with z in the radial range $0.3 \leq r/R_{200m} \leq 2$. While the gas density roughly traces the DM density in this radial range, there is 10%–20% deviation in the gas-to-DM density ratio from the cosmic value around the accretion shock. The value of $\rho_{\text{gas}}/\rho_{\text{DM}}$ is below the cosmic value in the intermediate region ($0.6 \leq r/R_{200m} \leq 1$), but exceeds the cosmic value in the inner ($0.3 \leq r/R_{200m} \leq 0.6$) and outer ($1.0 \leq r/R_{200m} \leq 3$) regions of clusters, and asymptotically approaches the cosmic value beyond $3R_{200m}$. The deviation from the cosmic value is on average about 10% around the accretion shock, but could reach to more than 20% for individual clusters. This pattern in the $\rho_{\text{gas}}/\rho_{\text{DM}}$ profile originates from the difference in the dynamics between gas and DM discussed in Section 4.1. Shock heating and ram pressure cause gas to lag behind DM during infall, creating an overdensity of gas around the accretion shock R_{sh} , indicated by the peak in the $\rho_{\text{gas}}/\rho_{\text{DM}}$ profile. The collisionless DM, on the other hand, penetrates further into the inner region of the cluster, undergoes core passage, and accumulates at the first apocenter passage, leading to slightly overdense DM density at $r \sim R_{200m}$. This drop in DM densities from $1.0R_{200m}$ to $1.6R_{200m}$ corresponds to the “splashback” radius, where the outermost caustic of the DM is located (Diemer & Kravtsov 2014; Adhikari et al. 2014). Our work suggests that the “splashback” radius of DM coincides with the accretion shock radius of the gas. In the right panel of Figure 9, we also show the dependence of MAR in the profiles of the gas-

to-DM density ratio for the $z = 0$ clusters. The profiles follow the same pattern as in the left panel. The peak of the profiles occurs at smaller radii for clusters with the highest MAR.

Recently, Patej & Loeb (2015) proposed an analytical model of gas distribution in galaxy clusters that depends on the ratio of the gas density jump to DM density jump at the accretion shock. They find that fitting their model to observed gas density profiles infers a similar gas density jump to that of DM density around the accretion shock, consistent with our findings that the gas density traces DM density to within $\lesssim 20\%$ in the cluster outskirts. Their model can be further improved by considering the effect of differential dynamics between the collisionless DM and collisional gas that leads to the deviation of the gas-to-DM density ratio from the cosmic mean. This will provide an unique approach for constraining the physics of cluster accretion shocks based on observations of the inner ICM profiles.

4.5. Location of the Accretion Shock

The dependence of outskirts gas profiles on α_{200m} is similar to that of z for $\Delta_c = 200$ (see Figures 2 and 3). The accretion shock occurs closer to the cluster center for systems with more negative values of α_{200m} . Similarly, for $\Delta_c = 200$, high- z clusters on average have their accretion shock closer to the cluster center. This suggests that the apparent evolution of the profiles for $\Delta_c = 200$ originates from the evolution in the *physical* MAR, where high- z clusters experience more rapid mass accretion than low- z counterparts. Normalizing clusters with respect to $\Delta_m = 200$ accounts for the redshift dependence of effects of the average MAR on the outskirts gas profiles, while the residual differences in MAR between clusters at a given redshift contribute to the scatter in the profiles. We further investigate how the location of the accretion shock depends on redshift, mass, and accretion rate. In Figure 10, we characterize the relationship between the location of the accretion shock R_{sh} in units of R_{200m} and the MAR proxy α_{200m} . We divide the cluster sample into a high and low peak height bin,

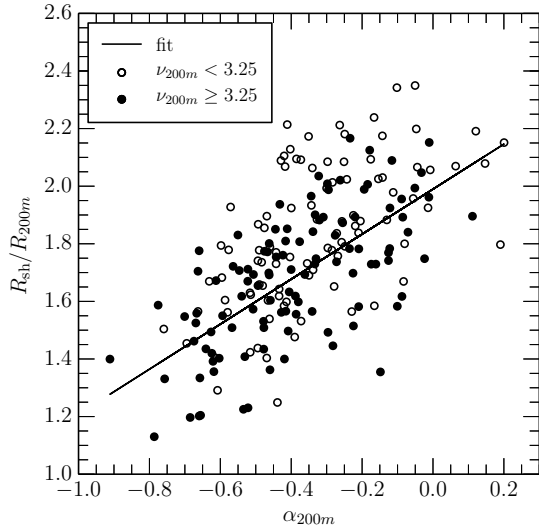


Figure 10. Relation between the shock radius R_{sh}/R_{200m} and the MAR α_{200m} of clusters at $z = 0.0, 0.5, 1.0, 1.5$ binned by their peak heights ν_{200m} . The filled and empty points represent clusters with ν_{200m} greater than or less than 3.25, respectively. The line represents the best-fit $R_{\text{sh}}/R_{200m} - \alpha_{200m}$ relation.

splitting at $\nu_{200m} = \delta_c / \sigma(M_{200m}, z) = 3.25$. The accretion shock radius R_{sh}/R_{200m} has a linear correlation that is independent of peak height. Halos with different peak height occupy different regions along the relation, where low peak height halos tend to have slightly larger R_{sh}/R_{200m} and low MAR (more positive α_{200m}), although this trend is fairly weak.

We quantify the best-fit relation between R_{sh}/R_{200m} and α_{200m} by performing linear least square fit:

$$R_{\text{sh}}/R_{200m} = A + B\alpha_{200m} \quad (12)$$

where $A = 1.990 \pm 0.030$ and $B = 0.782 \pm 0.067$. Note that this accretion shock radius is considerably larger than R_{200c} ($\approx 0.6R_{200m}$ at $z = 0$), or the virial radius R_{vir} ($\approx 0.8R_{200m}$ at $z = 0$). This redshift independent location of the accretion shocks should be useful for modeling how accretion shocks generate non-thermal pressure (Shi & Komatsu 2014), non-equilibrium electrons (e.g., Avestruz et al. 2014), and cosmic rays (see Brunetti & Jones 2014, for review), as well as assessing their effects on the hydrostatic mass bias (e.g., Laganá et al. 2010). Note further that we defined the shock radius using the peak of the azimuthally averaged entropy profile, while the actual topology of the accretion shock is quite complicated, which contributes to the large scatter in the $R_{\text{sh}}/R_{200m} - \alpha_{200m}$ relation.

5. CONCLUSIONS AND DISCUSSION

In this work we investigated the self-similarity of the diffuse X-ray emitting gas profiles in the outskirts of galaxy clusters using a mass-limited sample of simulated clusters extracted from the *Omega500* cosmological hydrodynamic simulation. Our main results are summarized below:

1. The radial profiles of the diffuse ICM in the outskirts of galaxy clusters at $r \gtrsim R_{200c} \approx 0.6R_{200m}$ exhibit remarkable self-similarity with redshift when they are normalized with respect to the mean density of the universe, while in the inner regions of clusters they are more

self-similar when normalized with respect to the critical density. This difference in the scaling property of the ICM radial profiles originates from the fact that the outer gas profiles are determined by late time accretion governed by the mean density of the universe, while the inner profiles are determined by the gravitational potential that is set when the universe is still matter-dominated and stays roughly constant afterward.

2. The diffuse ICM profiles in cluster outskirts depend on the mass accretion rate (MAR) of the cluster. To quantify the MAR, we proposed a new indicator α which is defined as the ratio of the local infall dark matter (DM) velocity in the halo outskirts to the virial velocity of the halo. Using this new indicator, we find that the pressure and temperature profiles of low MAR clusters are systematically higher than those of high MAR clusters, because a significant fraction of kinetic energy associated with accreting materials has not yet been thermalized in rapidly accreting clusters. Specifically, our results suggest that the ICM pressure profile is not “universal” at large radii when scaled to R_{200c} . While the pressure profile in cluster outskirts exhibits a more universal evolution when scaled to R_{200m} , the profile at large radii is generally sensitive to MAR. Therefore, any use of the “universal” pressure profile in extrapolating thermal SZ measurements from the outskirts to R_{500c} will likely be biased. This is especially important when the beam size of the instrument is too large to resolve R_{500c} for high- z clusters, e.g., as in the case of *Planck*. Our work suggests that the effects of MAR must be taken into account when interpreting SZ observations of cluster outskirts, including the recent *Planck*’s stacked SZ measurements which detected thermal pressure profiles around massive clusters out to $3 \times R_{500c} \approx 1.2R_{200m}$ (Planck Collaboration Int. V 2013).
3. Gas does not trace DM perfectly in the infall regions of galaxy clusters, because the collisional gas accretes slower than the collisionless DM. This causes the gas-to-DM density ratio to deviate from the cosmic mean value by about 10% near the accretion shocks, and steepens the gas density profile relative to the DM profile at large cluster-centric radii. Recent ultra-deep ($\gtrsim 2$ Ms) *Chandra* observation of Abell 133 and Abell 1795 (Vikhlinin et al., in prep.) may be able to detect the steepening in X-ray emissions in the diffuse ICM component, after properly removing point sources, clumps, and filaments.
4. The accretion shock radius R_{sh} is on average located at the fixed fraction of R_{200m} ($R_{\text{sh}}/R_{200m} \approx 1.6$) of galaxy clusters independent of redshift ($0 \leq z \leq 1.5$). However, there is also a large scatter in the accretion shock radius ($R_{\text{sh}}/R_{200m} \approx 1.0 - 2.4$), depending on the MAR of clusters. Higher MAR clusters have smaller accretion shock radius. These results can be useful for modeling physical processes (such as generation of turbulence and cosmic-rays) related to accretion and shock heating at outer boundaries of galaxy clusters.
5. Our results suggest that the critical density is still preferred in defining cluster mass and radius, for calibrations of observable-mass relations (e.g., $M - Y_X$ and $M - Y_{\text{SZ}}$) based on the current generation of X-ray and

SZ profile measurements, which mostly probe gas out to $r \lesssim R_{500c}$. Since the outer profiles are more self-similar when they are normalized with respect to the mean mass density, the exploitation of cluster outskirts for cosmology requires some care. For example, using the critical density in normalizing the outer ICM profiles can introduce redshift-dependent systematic biases in cluster scaling relations. Furthermore, scaling relations of cluster outskirts are expected to show larger scatter due to variations in MAR. Detailed understanding of physical processes and observational biases will be critical for interpreting data from the next-generation of X-ray and SZ missions, such as *SMART-X*³ and *Athena+*⁴.

We thank Benedikt Diemer, Oleg Gnedin, Eiichiro Komatsu, Andrey Kravtsov, Avi Loeb, Xun Shi, Andrew Wetzel, and the anonymous referee for useful discussion and/or comments on the manuscript. This work was supported in part by NSF grants AST-1412768 & 1009811, NASA ATP grant NNX11AE07G, NASA Chandra grants GO213004B and TM4-15007X, the Research Corporation, and by the facilities and staff of the Yale University Faculty of Arts and Sciences High Performance Computing Center. CA acknowledges support from the NSF Graduate Student Research Fellowship and Alan D. Bromley Fellowship from Yale University.

REFERENCES

- Adhikari, S., Dalal, N., & Chamberlain, R. T. 2014, JCAP, 11, 19
 Akamatsu, H., Hoshino, A., Ishisaki, Y., et al. 2011, PASJ, 63, 1019
 Allen, S. W., Evrard, A. E., & Mantz, A. B. 2011, ARA&A, 49, 409
 Arnaud, M., Pratt, G. W., Piffaretti, R., et al. 2010, A&A, 517, A92
 Avestruz, C., Nagai, D., Lau, E. T., & Nelson, K. 2014, ApJ, accepted, arXiv:1410.8142
 Bautz, M. W., Miller, E. D., Sanders, J. S., et al. 2009, PASJ, 61, 1117
 Bertschinger, E. 1985, ApJS, 58, 39
 Brunetti, G., & Jones, T. W. 2014, IJMPD, 23, 30007
 Bryan, G. L., & Norman, M. L. 1998, ApJ, 495, 80
 Cavaliere, A., Lapi, A., & Fusco-Femiano, R. 2011, ApJ, 742, 19
 Cuesta, A. J., Prada, F., Klypin, A., & Moles, M. 2008, MNRAS, 389, 385
 Diemer, B., & Kravtsov, A. V. 2014, ApJ, 789, 1
 Eckert, D., Molendi, S., Vazza, F., Ettori, S., & Paltani, S. 2013, A&A, 551, A22
 Faucher-Giguère, C.-A., Kereš, D., & Ma, C.-P. 2011, MNRAS, 417, 2982
 George, M. R., Fabian, A. C., Sanders, J. S., Young, A. J., & Russell, H. R. 2009, MNRAS, 395, 657
 Hoshino, A., Henry, J. P., Sato, K., et al. 2010, PASJ, 62, 371
 Jenkins, A., Frenk, C. S., White, S. D. M., et al. 2001, MNRAS, 321, 372
 Kaiser, N. 1986, MNRAS, 222, 323
 Kawaharada, M., Okabe, N., Umetsu, K., et al. 2010, ApJ, 714, 423
 Klypin, A., Kravtsov, A. V., Bullock, J. S., & Primack, J. R. 2001, ApJ, 554, 903
 Kravtsov, A. V. 1999, PhD thesis, New Mexico State Univ.
 Kravtsov, A. V., & Borgani, S. 2012, ARA&A, 50, 353
 Kravtsov, A. V., Klypin, A., & Hoffman, Y. 2002, ApJ, 571, 563
 Kravtsov, A. V., Vikhlinin, A., & Nagai, D. 2006, ApJ, 650, 128
 Laganá, T. F., de Souza, R. S., & Keller, G. R. 2010, A&A, 510, A76
 Li, Y., Mo, H. J., van den Bosch, F. C., & Lin, W. P. 2007, MNRAS, 379, 689
 Maughan, B. J. 2007, ApJ, 668, 772
 McBride, J., Fakhouri, O., & Ma, C.-P. 2009, MNRAS, 398, 1858
 McCourt, M., Quataert, E., & Parrish, I. J. 2013, MNRAS, 432, 404
 McDonald, M., Benson, B. A., Vikhlinin, A., et al. 2014, ApJ, 794, 67
 Molnar, S. M., Hearn, N., Haiman, Z., et al. 2009, ApJ, 696, 1640
 Morandi, A., Sun, M., Forman, W., & Jones, C. 2015, MNRAS, in press, arXiv:1501.04095
 Nagai, D., Kravtsov, A. V., & Vikhlinin, A. 2007, ApJ, 668, 1
 Nagai, D., & Lau, E. T. 2011, ApJL, 731, L10
 Nelson, K., Lau, E. T., & Nagai, D. 2014a, ApJ, 792, 25
 Nelson, K., Lau, E. T., Nagai, D., Rudd, D. H., & Yu, L. 2014b, ApJ, 782, 107
 Nelson, K., Rudd, D. H., Shaw, L., & Nagai, D. 2012, ApJ, 751, 121
 Okabe, N., Umetsu, K., Tamura, T., et al. 2014, PASJ, 66, 99
 Parrish, I. J., McCourt, M., Quataert, E., & Sharma, P. 2012, MNRAS, 419, L29
 Patej, A., & Loeb, A. 2015, ApJL, 798, L20
 Pfrommer, C., Springel, V., Enßlin, T. A., & Jubelgas, M. 2006, MNRAS, 367, 113
 Planck Collaboration Int. V. 2013, A&A, 550, A131
 Planelles, S., & Quilis, V. 2013, MNRAS, 428, 1643
 Pratt, G. W., Croston, J. H., Arnaud, M., & Böhringer, H. 2009, A&A, 498, 361
 Rasia, E., Lau, E. T., Borgani, S., et al. 2014, ApJ, 791, 96
 Reiprich, T. H., Basu, K., Ettori, S., et al. 2013, SSRv, 177, 195
 Reiprich, T. H., Hudson, D. S., Zhang, Y.-Y., et al. 2009, A&A, 501, 899
 Roncarelli, M., Ettori, S., Borgani, S., et al. 2013, MNRAS, 432, 3030
 Rudd, D. H., & Nagai, D. 2009, ApJL, 701, L16
 Rudd, D. H., Zentner, A. R., & Kravtsov, A. V. 2008, ApJ, 672, 19
 Ryu, D., Kang, H., Hallman, E., & Jones, T. W. 2003, ApJ, 593, 599
 Schaal, K., & Springel, V. 2015, MNRAS, 446, 3992
 Shi, X., & Komatsu, E. 2014, MNRAS, 442, 521
 Shi, X., Komatsu, E., Nelson, K., & Nagai, D. 2015, MNRAS, 448, 1020
 Simionescu, A., Allen, S. W., Mantz, A., et al. 2011, Sci, 331, 1576
 Skillman, S. W., O'Shea, B. W., Hallman, E. J., Burns, J. O., & Norman, M. L. 2008, ApJ, 689, 1063
 Tinker, J., Kravtsov, A. V., Klypin, A., et al. 2008, ApJ, 688, 709
 Tozzi, P., & Norman, C. 2001, ApJ, 546, 63
 Urban, O., Simionescu, A., Werner, N., et al. 2014, MNRAS, 437, 3939
 van de Voort, F., Schaye, J., Booth, C. M., Haas, M. R., & Dalla Vecchia, C. 2011, MNRAS, 414, 2458
 van den Bosch, F. C., Jiang, F., Hearin, A., et al. 2014, MNRAS, 445, 1713
 Vazza, F., Brunetti, G., & Gheller, C. 2009a, MNRAS, 395, 1333
 Vazza, F., Brunetti, G., Kritsuk, A., et al. 2009b, A&A, 504, 33
 Vazza, F., Eckert, D., Simionescu, A., Brügggen, M., & Ettori, S. 2013, MNRAS, 429, 799
 Vikhlinin, A., Kravtsov, A., Forman, W., et al. 2006, ApJ, 640, 691
 Voit, G. M. 2005, RvMP, 77, 207
 Voit, G. M., Balogh, M. L., Bower, R. G., Lacey, C. G., & Bryan, G. L. 2003, ApJ, 593, 272
 Walker, S. A., Fabian, A. C., Sanders, J. S., Simionescu, A., & Tawara, Y. 2013, MNRAS, 432, 554
 Wechsler, R. H., Bullock, J. S., Primack, J. R., Kravtsov, A. V., & Dekel, A. 2002, ApJ, 568, 52
 Wetzel, A. R., & Nagai, D. 2014, ApJ, submitted, arXiv:1412.0662
 White, M. 2002, ApJS, 143, 241
 Wu, H.-Y., Hahn, O., Wechsler, R. H., Mao, Y.-Y., & Behroozi, P. S. 2013, ApJ, 763, 70
 Zhao, D. H., Mo, H. J., Jing, Y. P., & Börner, G. 2003, MNRAS, 339, 12
 Zhuravleva, I., Churazov, E., Kravtsov, A., et al. 2013, MNRAS, 428, 3274

³ <http://smart-x.cfa.harvard.edu/>

⁴ <http://athena2.irap.omp.eu/>